ChemElectroChem

Research Article
doi.org/10.1002/celc.202500237

Chemistry Europe
European Chemical Societies Publishing

www.chemelectrochem.org

Influence of State-of-Charge-Dependent Decomposition Kinetics at the $Li_6PS_5Cl|LiNi_{0.83}Co_{0.11}Mn_{0.06}O_2$ Interface on Solid-State Battery Performance

Melina Witt, Martin A. Lange, and Wolfgang G. Zeier*

Solid-state batteries represent a new approach to energy storage, offering superior safety, higher energy density, and extended cycle life compared to conventional liquid electrolyte-based lithium-ion batteries. However, the practical application of solid-state batteries is hindered by degradation phenomena, particularly on interfaces between components, compromising their long-term performance. In this work, the kinetics of the state-of-charge-dependent electrolyte degradation at the $LiNi_{0.83}Co_{0.11}Mn_{0.06}O_2 \mid Li_6PS_5Cl$ interface, as well as its influence on cycling performance, are systematically studied electrochemically in solid-state battery half cells. Combining cycling and C-rate experiments with electrochemical impedance spectroscopy reveals that half cells charged to higher cutoff potentials ($\geq$3.8 V versus In/InLi; $\geq$4.4 V versus Li^+/Li) exhibit significantly faster degradation kinetics. These influence the cycling performance leading to a plateau in the charge capacity at $\geq$3.8 V versus In/InLi, while the electrolyte degradation does not affect the bulk electrode transport. Overall, this work emphasizes the importance to investigate state-of-charge-dependent decomposition kinetics in composite electrodes to better understand cycling behavior.

1. Introduction

Currently, lithium-ion batteries remain the most widely used energy storage systems.[1] However, due to their higher energy densities, their suggested enhanced intrinsic safety and their wider operating temperature window, solid-state batteries using inorganic solid electrolytes (SEs) have been emerging as a promising alternative.[2,3] Although various SEs like oxides,[4,5] halides,[6,7] and oxyhalides[8,9] have been investigated in the past decades, thiophosphate-based argyrodites, such as Li_6PS_5Cl (LPSCl), are among the most widely used electrolyte classes due to their high ionic conductivity.[10–12] Achieving sufficient high energy and high-power densities in solid-state batteries, however, requires high-capacity cathode active materials (CAM). One of the most commonly used CAM classes is the nickel-rich layered lithium transition metal oxides $LiNi_{1-x-y}Co_xMn_yO_2$ (NCM) which exhibit a high cycling stability in solid-state batteries.[13–15]

Due to the narrow electrochemical stability window of lithium thiophosphate SEs,[16,17] the simultaneous use of both lithium argyrodites and NCM cathode material leads to severe decomposition processes within the composite.[18,19] This interfacial instability can lead to compromised ion conductivity, resulting in increased internal resistance[20] and, consequently, in a loss of capacity over cycling.[21] The great dependency of the cycling behavior of solid-state batteries on stability highlights that controlling operational parameters, such as the cutoff potential, is important to optimize battery performance.

Various studies have shown that operating at higher cutoff potentials can enhance the accessible capacity but may also accelerate degradation mechanisms such as phase transitions,[22] electrolyte decomposition,[23] and structural collapse of the catholyte or CAM.[24] Investigation of β–Li_3PS_4: $LiNi_{0.8}Co_{0.1}Mn_{0.1}O_2$ composites at varying cutoff potentials from 3.4 to 4.4 V versus In/InLi by Koerver et al. suggests that the interfacial resistance at the cathode is partly dependent on the battery's state of charge (SOC), aligning with the notion of a redox-active cathode electrolyte interphase (CEI) layer. The thickness of this layer increases with the cutoff potential and corresponds to increasing capacity fading.[25] The correlation of the interface evolution and SOC in a $Li_{10}GeP_2S_{12}$:$LiNi_{0.6}Co_{0.2}Mn_{0.2}O_2$ (LGPS|NCM–622) composite was investigated by Zuo et al., applying upper cutoff potentials between 3.1 V and 3.9 V versus In/InLi, in order to understand the reactivity and the degradation kinetics. In this system, the degradation rate of the electrolyte/electrode interface showed an increase with higher SOC. In addition, the growth of the corresponding degradation layer proved to be limited by the

---

M. Witt, M. A. Lange, W. G. Zeier
Institute of Inorganic and Analytical Chemistry
University of Münster
Corrensstrasse 28/30, 48149 Münster, Germany
E-mail: wzeier@uni-muenster.de

M. A. Lange, W. G. Zeier
Institute of Energy Materials and Devices (IMD)
IMD-4: Helmholtz-Institut Münster
Forschungszentrum Jülich Corrensstrasse 48, 48149 Münster, Germany

Supporting information for this article is available on the WWW under https://doi.org/10.1002/celc.202500237

electronic transport.[19] Similarly, Hartel et al. explored Zn^{2+} substitution in lithium argyrodites as SEs for solid-state batteries, aiming to modify the CEI to improve battery performance. Higher Zn^{2+} content facilitates degradation kinetics and leads to increased CEI resistance, suggesting that while Zn^{2+} impacts the structure and transport of the SE, it may also accelerate decomposition processed at higher potentials.[26] Furthermore, Morino analyzed the degradation rate of the interface in a LPSCl:$LiNbO_3$-coated $LiNi_{0.5}Co_{0.2}Mn_{0.3}O_2$ composite, varying the upper cutoff potential from 3.63 to 3.93 V versus In/InLi. The study revealed that the capacity fading depends on the extent of interfacial decomposition and that the activation energy of the cell degradation constant behaves antiproportional to the cutoff potential.[27] Understanding the degradation kinetics of cathode composites at different cutoff potentials is essential to unlock the full potential of solid-state batteries by counteracting detrimental behavior/processes. Degradation processes, including interfacial reactions, phase transition, and mechanical failures, directly impact the cycle life, rate performance, and overall reliability of these batteries. Yet, the mechanisms driving these degradation processes remain poorly understood.

This study aims to provide a template to systematically investigate the degradation kinetics of cathode composites to help improve this understanding. Herein, we use a $LiNi_{0.83}Co_{0.11}Mn_{0.06}O_2$ (NCM-83) cathode composite with LPSCl as catholyte and applying different upper cutoff potentials in the range of 3.4–3.9 V versus In/InLi, that is, 4.0–4.5 V versus Li^+/Li. By examining this system electrochemically, we seek to uncover the underlying mechanisms that influence the cathode stability and performance in this system to provide a base for further systematic optimization of the single components. In thoroughly analyzing the effects of cutoff potential on the systems cycling and C-rate performance, and by monitoring interphase formation at the LPSCl|NCM-83 interface as a function of time using electrochemical impedance spectroscopy (EIS), this work aims to identify optimal cycling conditions that maximize energy output while maintaining the electrochemical properties of the cathode. Utilizing the well-established correlation between SOC and internal resistance[19,20,25] (as shown in **Figure 1**a), this work uses an EIS measurement procedure to systematically analyze the CEI formation (Figure 1b). This procedure involves charging a cell to a defined upper cutoff potential between 3.4 V and 3.9 V versus In/InLi. The cells are continuously maintained at this potential for 24 h, with EIS performed at 30 min intervals to assess the time-dependent impact of the potential hold. Subsequently, the cell is cycled for 25 cycles at 0.1 C, with EIS conducted after each discharge and charge step to investigate the reversibility of certain processes upon the initial discharge and to examine the influence of different oxidative potentials on CEI formation during cycling.

This work demonstrates that the cycling performance, C-rate behavior, and the kinetics of the CEI formation are tightly linked to the SOC. While the obtained capacities are higher at increased cutoff potentials, a limit in obtained capacity is visible above a threshold of 3.8 V versus In/InLi. This is also visible at higher C-rates, implying better transport properties at higher potentials with higher current densities. In addition, EIS unveils two distinct jumps in the CEI growth rate after 3.6 V and 3.8 V versus In/InLi, which can be linked to the trends in cycling and C-rate performance. Overall, this work provides insights into the relationship of CEI formation and the SOC of nickel-rich CAM and helps understand the impact of the cutoff potential on solid-state battery cycling performance.

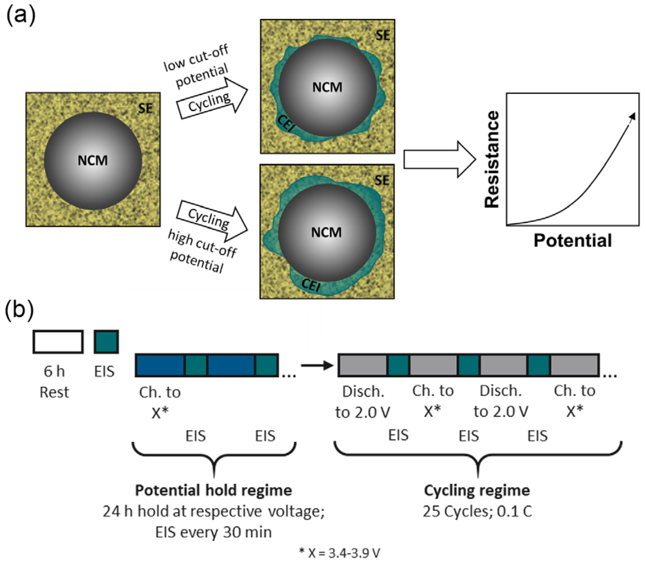

Figure 1. a) Illustration of the CEI growth at different cutoff potentials and the correlation between SOC and internal resistance. b) Schematic overview of the EIS measurement procedure carried out in this work. After an initial rest step, followed by a first EIS measurement, the cell is charged to a selected upper cutoff potential between 3.4 and 3.9 V versus In/InLi. This potential is held for 24 h, and EIS measurements are conducted every 30 min. After this 24 h potential hold regime, the cell is discharged to 2.0 V versus In/InLi and then cycled for 25 cycles in the potential range between 2.0 V and the selected upper cutoff potential, with EIS measurements carried out after each discharge and charge cycle. All measurements are performed at 25 °C at a C-rate of 0.1 C.

2. Results and Discussion

2.1. Solid-State Battery Cycling

The initial charge–discharge curves of one cell for each cutoff potential with 0.1 C are displayed in **Figure 2**a. Charge and discharge curves of selected cycles are exemplary shown for 3.4 V and 3.9 V versus In/InLi in Figure 2b. The charge and discharge curves of selected cycles for the other cutoff potentials are displayed in Figure S2, Supporting Information. The general shape of the curves during cycling is similar for all cutoff potentials. Upon initial charge, all curves show identical steadily increasing achieved capacities until the chosen cutoff potential is reached. This shows that the specific charge capacity is potential dependent and higher capacities can be expected for higher potentials (Figure S3, Supporting Information). The charge capacity fading during cycling at 3.4 V and 3.9 V versus In/InLi from first (159 ± 3 mAh·g^{-1} and 225 ± 7 mAh·g^{-1}) to 25th (126 ± 17 mAh·g^{-1}

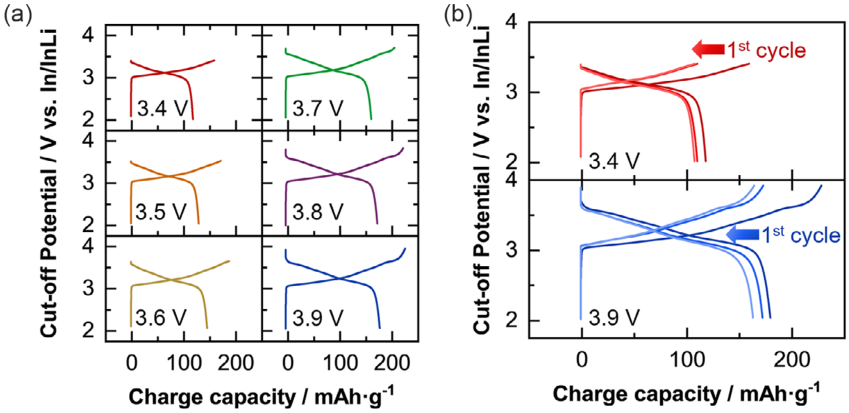

Figure 2. Cycling performance of In/InLi|Li_6PS_5Cl|NCM-83:Li_6PS_5Cl half-cells at different upper cutoff potentials between 3.4 V and 3.9 V versus In/InLi in 0.1 V steps. a) Showing the charge–discharge curves at 0.1 C of the 1st cycle, respectively. b) Charge discharge curves of the 1st, 25th, and 50th cycle for one cell of the upper cutoff potentials 3.4 V and 3.9 V versus In/InLi.

and 170 ± 3 mAh·g^{-1}) to 50th cycle (127 ± 20 mAh·g^{-1} and 162 ± 11 mAh·g^{-1}) seems to be stable after the initial cycle at all cutoff potentials. The discharge curves of cells cycled with an upper cutoff potential of 3.4 V and 3.9 V versus In/InLi exhibit a similar trend, meaning the obtained capacities drop during cycling from 116 ± 4 mAh·g^{-1} and 176 ± 8 mAh·g^{-1} (first cycle) to 109 ± 8 ;mAh·g^{-1} and 170 ± 12 mAh·g^{-1} (25th cycle) to 107 ± 7 mAh·g^{-1} and 161 ± 12 mAh·g^{-1} (50th cycle).

Figure 3a displays the average cycling performance of half-cells over 50 cycles at each upper cutoff potential between 3.4 V and 3.9 V versus In/InLi in 0.1 V steps with their respective standard deviation. The cycling data for all individual cells is depicted in the Supplementary Information Table S1 and Figure S4. The averaged initial specific charge capacities of the cells are 159 ± 3 mAh·g^{-1} (3.4 V), 174 ± 1 mAh·g^{-1} (3.5 V), 196 ± 7 mAh·g^{-1} (3.6 V), 212 ± 2 mAh·g^{-1} (3.7 V), 220 ± 5 mAh·g^{-1} (3.8 V), and 225 ± 7 mAh·g^{-1} (3.9 V), respectively. The observed capacity loss following the initial cycle is likely due to a combination of electrolyte decomposition, triggered by its instability in contact with the NCM, structural changes, and kinetic limitations during discharge.[28,29] The invariance of the averaged state of health with respect to cutoff potential (Table S1, Supporting Information) suggests that the capacity retention is independent of the applied upper cutoff potential. In contrast, the specific charge capacity increases with higher cutoff potentials, indicating more extensive lithium deintercalation from the cathode composite during cycling.[19] However, this trend does not persist beyond a cutoff potential of 3.8 V versus In/InLi, at which point the specific capacity reaches a plateau. This observation suggests that the maximum extent of lithium extraction from the cathode is achieved at 3.8 V, as no further increase in capacity is observed when charging to 3.9 V versus In/InLi. To show this in more detail, the capacity of selected cycles is shown against the respective cutoff potential in Figure 3b. The specific capacity increases until 3.8 V versus In/InLi, where it reaches a plateau. The C-rate performance tests (Figure 3c,d and Figure S5, Supporting Information) confirm this behavior, showing that although higher cutoff potentials improve charge capacity and rate performance, a maximum is reached at 3.8 V versus In/InLi across all C-rates. These results imply that the electrolyte degradation proceeds independently of the applied current density. However, the uncertainties of the obtained capacities increase with increasing C-rates. This emphasizes that contact loss between the SE and the electrode material, together with the transport limitation within the composite, has a greater influence at higher C-rates or that the higher C-rates may favor these transport limitations in the first place.[30] In Figure 3e, the rate dependency of the capacity is exemplarily described for one cell each (all cells are depicted in Figure S6, Supporting Information) with the semi-empirical fit (Equation 1[31]) recently introduced by Tian et al. and uses the practical rate r instead of the conventional C-rate. The practical rate (Equation 2[31]) considers the achieved capacity instead of the theoretical capacity of the CAM and is described by the applied current I and the experimental capacity at that current $Q_{exp}(I)$. This rate capability analysis has been recently adapted to solid-state batteries.[32,33]

$$Q_{CAM}(r) = Q_{CAM,0} \cdot \left(1 - (r\tau)^n \cdot \left(1 - e^{(-r\tau)^{-n}}\right)\right) \tag{1}$$

$$r = I/Q_{exp}(I) \tag{2}$$

The rate-dependent measured specific capacity is represented by $Q_{CAM}(r)$ and $Q_{CAM,0}$ corresponds to the low-rate specific capacity. The parameter τ describes the transition point from low-rate behavior to high-rate capacity decay and the parameter n describes the slope of the accelerated capacity decay at high practical rates. The averaged values of τ and n obtained from this fit are presented in Figure 3f for all cutoff potentials. The determined τ and n values (Table S2 and S3, Supporting Information) are in a similar range for all cutoff potentials, indicating a similar rate performance. Thus, implying the electrolyte degradation does not influence the transport within the electrode.

2.2. Electrochemical Impedance Spectroscopy

The underlying cause for the different cycling performance over 50 cycles and the C-rate performance requires a more thorough investigation. Therefore, the degradation of the composite

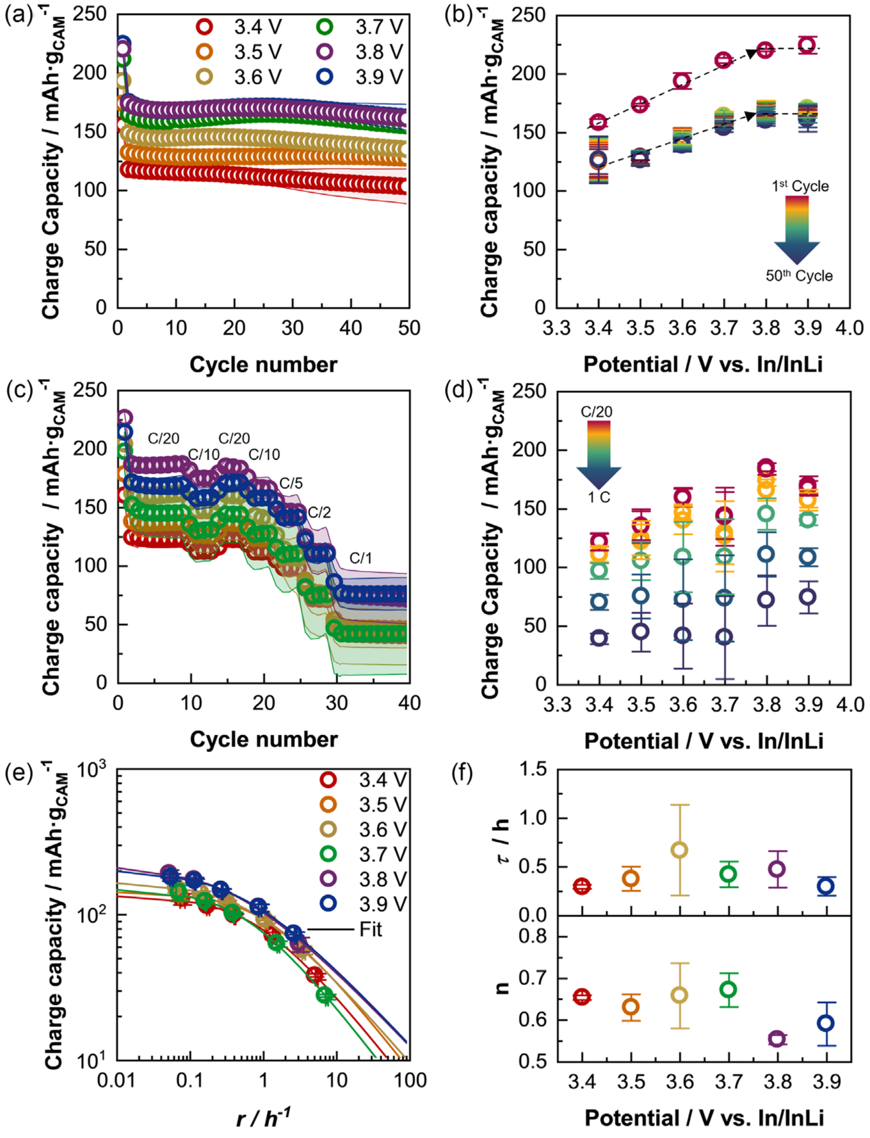

Figure 3. Cycling performance of In/InLi|LPSCl|NCM-83:LPSCl half-cells at different upper cutoff potentials between 3.4 V and 3.9 V versus In/InLi in 0.1 V steps. a) Averaged charge capacities of triplicates cycled for 50 cycles at 0.1 C ($j = 0.214$ mA·cm^{-2}), respectively. b) Charge capacities plotted against the cutoff potential for every fifth cycle, respectively. c) Averaged C-rate performance test In/InLi|LPSCl|NCM-83:LPSCl half-cell triplicates at different upper cutoff potentials between 3.4 V and 3.9 V versus In/InLi in 0.1 V steps. d) Average charge capacities plotted against the cutoff potential for every C-rate step, excluding the initial cycle, respectively. e) Specific charge capacity versus rate for the data taken from averaged rate capability exemplarily shown for one cell each and f) n and τ values gained from the fit with Equation (1).

materials at contact points of NCM-83 and LPSCl,[18,19] along with the formation of a CEI layer, is evaluated at all cutoff potentials using EIS. The measurement procedure, schematically described in Figure 1b, is split into two parts for the following discussion, the potential hold regime and the cycling regime.

2.2.1. Potential Hold Regime

Representative electrochemical impedance spectra recorded during the potential hold regime are depicted in **Figure 4**, while the other spectra and the corresponding Bode plots for the measurements after 30 min and 24 h for all potentials are displayed in Figure S7 and S8, Supporting Information. Figure 4a,b shows the impedance spectra for a 3.4 V versus In/InLi cutoff potential after 30 min and 24 h, respectively. In addition, the equivalent circuit used for fitting every single impedance spectrum is depicted, assuming five different underlying processes in the system. The equivalent circuit, which allowed a reasonable fit, consists of a preresistance, three (RQ) elements, and a constant phase element (CPE). The capacitances of the fitted RQ-elements were compared with those of typical processes in solid-state batteries,[25,34] which lead to the following assignment: The first process corresponds to the bulk resistance within the SE, denoted as $R_{SE,bulk}$. The partial impedance at the grain boundaries within the SE is represented as $R_{SE,grain}$. The interface between the SE and the CAM is characterized by the partial impedance $R_{SE/CAM}$, whereas the interface

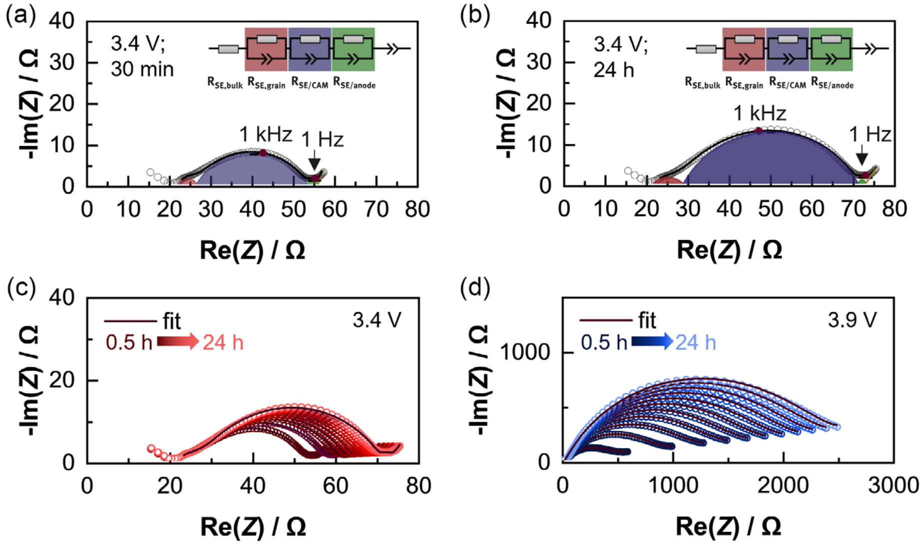

Figure 4. Nyquist plots of EIS data during the 24 h potential hold. The equivalent circuit used for fitting and the microscopic transport/transfer steps, which are assigned to the semicircles $R_{\mathrm{SE,grain}}$ (red), $R_{\mathrm{SE/CAM}}$ (purple) and $R_{\mathrm{SE/anode}}$ (green), are shown in two exemplary spectra for 3.4 V versus In/InLi after a) 30 min and b) 24 h of potential hold. The evolution of the total impedance during the 24 h of potential hold with measurements every 30 min is displayed for c) 3.4 V versus In/InLi and d) 3.9 V versus In/InLi over every 2.5 h from 30 min to 24 h.

between the SE and the anode is represented by the partial impedance $R_{\mathrm{SE/anode}}$. Lastly, a constant phase element (CPE) is incorporated in the low frequency range to model the Li^{+} diffusion into the electrode. The time-dependent increase in total resistance is mainly driven by the growth of the SE|CAM interface resistance ($R_{\mathrm{SE/CAM}}$), likely resulting from electrolyte degradation at the interface. This indicates that the degradation reactions at the LPSCl|NCM-83 interface do not stop with time, which is visible throughout the potential hold (Figure 4c) and is even more pronounced for the higher upper cutoff potentials (Figure S7, Supporting Information, and Figure 4d). Clearly, the degradation is SOC dependent for this system and therefore enables monitoring and extraction of the kinetics of the CEI formation at the different SOCs.

Based on this degradation behavior over time and the correlation between resistance and $t^{0.5}$, the CEI growth rate can be determined for each SOC.[19] For this established correlation, a Wagner-type model is employed to describe the diffusion-controlled degradation, which correlates the growth rate of the CEI to the migration of ionic and electronic charge carriers.[19] Assuming that the partial conductivities and the chemical potential of Li across the CEI layer within a cell remain relatively constant during the measurement, we can apply Equation (3)[19] to describe the correlation of the CEI resistance and $t^{0.5}$.

$$R_{\mathrm{CEI}} = \frac{1}{S\sigma_{\mathrm{CEI}}} \cdot \sqrt{\frac{V_{\mathrm{m}}}{xF^{2}} \cdot \frac{\sigma_{\mathrm{Li}^{+}} \cdot \sigma_{\mathrm{e}^{-}}}{\sigma_{\mathrm{Li}^{+}} + \sigma_{\mathrm{e}^{-}}} \cdot \Delta\mu_{\mathrm{Li}}} \cdot \sqrt{t} = \frac{1}{S\sigma_{\mathrm{CEI}}} \cdot \mathrm{k}\sqrt{t} = \mathrm{k}^{*}\sqrt{t} \tag{3}$$

In this equation, S represents the contact area, σ_{CEI} describes the average ionic conductivity, and V_{m} denotes the average molar volume of the CEI layer. The variable x quantifies the number of moles of Li extracted from LPSCl, while F corresponds to Faraday's constant. σ_{Li}^{+} and σ_{e}^{-} describe the mean partial ionic and electronic conductivities. The chemical potential difference of Li across the CEI layer, which acts as the driving force for the CEI growth, is represented by $\Delta\mu_{\mathrm{Li}}$. The growth rate, in relation to the thickness, is indicated by the rate constant k, while the further simplified growth rate in relation to resistance is represented by k^{*}, respectively. The dependance of the partial resistance $R_{\mathrm{SE/CAM}}$ on $t^{0.5}$ is displayed in **Figure 5**a for the upper cutoff potentials 3.4–3.9 V versus In/InLi, exhibiting near-linear behavior. This shows that not only the total resistance but mostly $R_{\mathrm{SE|CAM}}$ increases with time and increasing cutoff potential. The slope of the fitted linear behavior can then be correlated with the growth rate k^{*} of the interface between the SE and the CAM (Equation (3)). This interface growth rate k^{*}, presented in Figure 5b, increases relatively slowly up to an upper cutoff potential of 3.6 V versus In/InLi ($10.9 \pm 0.8\,\Omega\,\mathrm{h}^{-0.5}$), where a sudden increase to 3.7 V versus In/InLi ($61.3 \pm 1.1\,\Omega{\cdot}\mathrm{h}^{-0.5}$) can be observed. Between 3.8 V ($76.3 \pm 1.4\,\Omega{\cdot}\mathrm{h}^{-0.5}$) and 3.9 V versus In/InLi ($439.4 \pm 6.9\,\Omega{\cdot}\mathrm{h}^{-0.5}$), an even more significant increase is visible. These steep increases in growth rate denote that the degradation of the SE in contact with NCM-83, and with that, the formation of a CEI proceeds slowly at 3.4 V versus In/InLi and faster with increasing cutoff potential. This may indicate that the degradation products itself change as a function of SOC, further corroborating the suggestion by Zuo et al. that the amount of sulfate/sulfite (SO_3^{-}) and phosphate (PO_3^{-}) fragments increases with elevating potential.[19] In general, the growth rate k^{*} is larger over all cutoff potentials compared to LGPS|NCM-622 composites,[19] suggesting that the decomposition products formed at the LPSCl|NCM-83 interface are more detrimental for the lithium-ion transport. Interestingly, when compared to $\mathrm{Li}_{5.5}\mathrm{PS}_{4.5}\mathrm{Cl}_{1.5}$|NCM-83 or $\mathrm{Li}_{5.3}\mathrm{Zn}_{0.1}\mathrm{PS}_{4.5}\mathrm{Cl}_{1.5}$|NCM-83 composites,[26] the growth rates k^{*} seem to be similar up to 3.5 V versus In/InLi. However, the growth rate k^{*} is higher for LPSCl|NCM-83

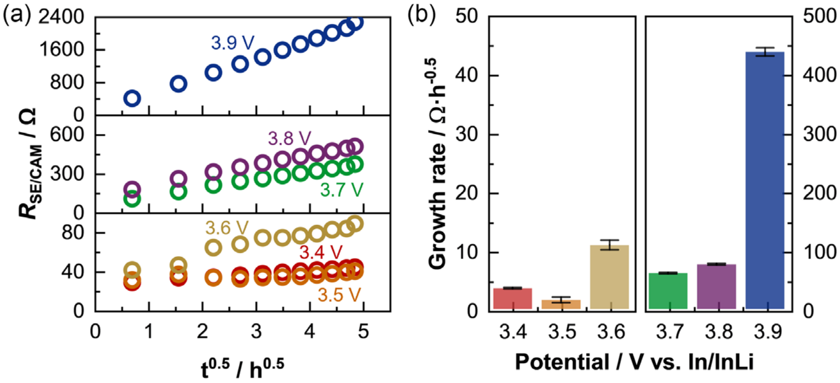

Figure 5. The resistance $R_{SE/CAM}$ extracted from the fitted impedance data for the upper cutoff potentials a) 3.4 V–3.9 V versus In/InLi over the square root of time $t^{0.5}$. The growth rate which can be extracted from the slope shown in (a) is displayed in (b).

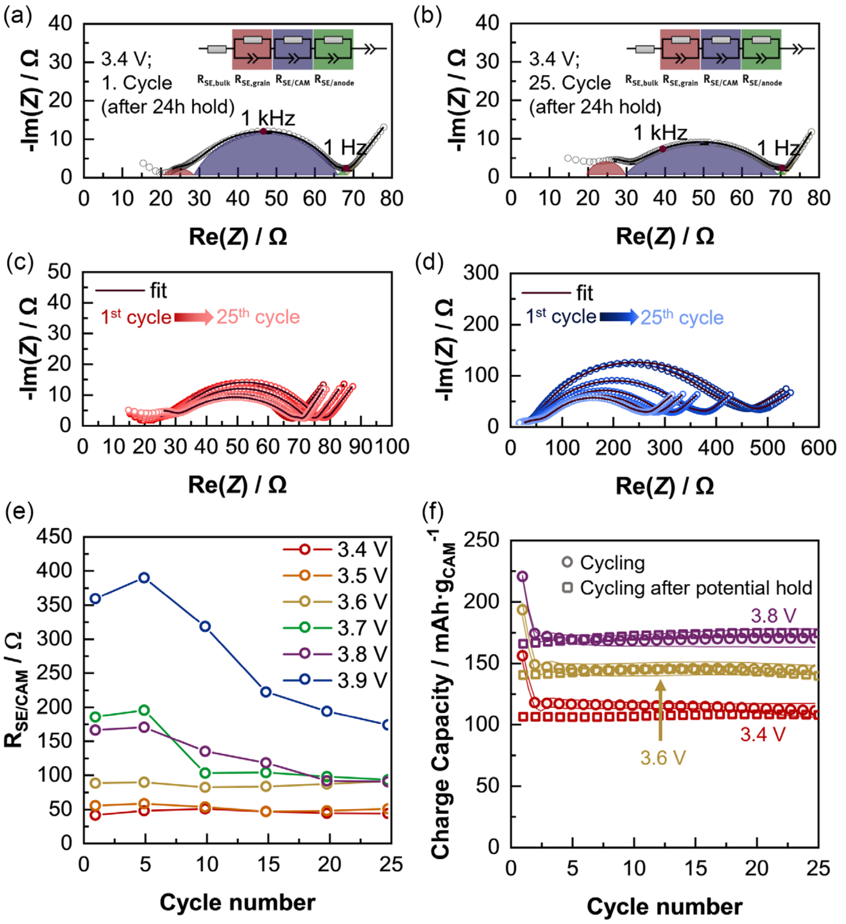

Figure 6. a–d) Nyquist plots of EIS data during cycling regime after the 24 h potential hold regime. The equivalent circuits used for fitting and the microscopic transport/transfer steps assigned to the semicircles $R_{SE,grain}$ (red), $R_{SE/CAM}$ (purple), and $R_{SE/anode}$ (green) are shown in two exemplary spectra for 3.4 V versus In/InLi after a) the first and b) the 25th cycle after the potential hold. The evolution of the total impedance during cycling regime is displayed for every fifth cycle from first to the 25th cycle of c) 3.4 V versus In/InLi and d) 3.9 V versus In/InLi. The resistance $R_{SE/CAM}$ extracted from the fitted impedance data for all upper cutoff potentials over every fifth cycle from the first cycle to the 25th cycle is shown in (e) and the capacities during the cycling performance of the cycling regime is compared with the first 25 cycles of the cycling performance over 50 cycles for the cutoff potentials 3.4 V, 3.6 V and 3.8 V versus In/InLi.in (f).

composites at 3.7 V versus In/ and lower at higher cutoff potentials. This suggests that the lower amount of chloride—and with it more sulfide—in the catholyte LPSCl affects the degradation kinetics, which is in accordance to the findings of Zuo et al.,[35] who could determine different amounts of the decomposition products when comparing these two SEs.

2.2.2. Cycling Regime

The cycling regime, which contains cycling the cell for 25 cycles after holding the respective upper cutoff potential for 24 h and keeping the cells in a charged state, is exemplarily shown for 3.4 V and 3.9 V versus In/InLi in **Figure 6**. The cycling regime for the other potentials is displayed in Figure S9, Supporting Information, and the Bode plots of the measurements after 30 min and 24 h for all potentials are depicted in Figure S10, Supporting Information. Figure 6a,b shows the impedance spectra for a 3.4 V versus In/InLi cutoff potential after the first and the 25th cycle, respectively, and the equivalent circuit used for fitting every single impedance spectrum, which is the same as used during the potential hold regime. A comparison of the impedance spectra after each cycle (Figure 6c,d and Figure S9, Supporting Information) shows that the overall resistance increases with elevating cutoff potential. The total resistance remains approximately the same or rises slightly with increasing number of cycles for the cutoff potentials up to 3.5 V versus In/InLi. At higher cutoff potentials, the total resistance decreases during cycling. However, when looking at the resistance $R_{\mathrm{SE|CAM}}$ associated with the SE|CAM interface (Figure 6e), it seems that it stays similar within a cutoff potential up to 3.6 V versus In/InLi, while it decreases for the higher cutoff potentials in the first cycles until it reaches a plateau. The results might indicate that the degradation of the SE in contact with NCM-83 and the associated CEI formation predominantly occurred during the 24 h potential hold at cutoff potentials of 3.4 V and 3.6 V versus In/InLi. In contrast, at higher cutoff potentials, these processes appear to continue during subsequent cycling. Comparing the resulting internal resistances of the 24 h potential hold regime (Figure 4c,d) with those of the first cycle afterward (Figure 6c,d), it becomes clear that it significantly decreases upon the start of cycling. This leads to the assumption that the decomposition is partially reversible, as previously stated from Auvergniot et al.[21] and Koerver et al.[25] Suggesting that the CEI formed during degradation is redox active. Integrating the findings from both the potential hold and cycling regimes suggests that higher cutoff potentials accelerate the CEI growth rate through intensified electrolyte decomposition, resulting in increased accumulation of SO_3^- and PO_3^- fragments. These interfacial changes are likely key contributors to the enhanced capacities observed at higher cutoff potentials. When comparing the capacities reached during the charge steps of the cycling regime with those of the cells that have been cycled for 50 cycles without the potential hold (Figure 3a), a similar trend and values can be observed. This is exemplarily depicted in Figure 6f for 3.4 V, 3.6 V, and 3.8 V versus In/InLi (Figure S11, Supporting Information, contains all cutoff potentials). It shows that cells with a potential hold regime prior to the cycling regime do not exhibit the capacity drop after the first cycle, which is visible for cells without a prior potential hold. This suggests that the processes responsible for the initial capacity loss occur during the potential hold regime. Both cycling methods reach a similar capacity region after a few cycles for all cutoff potentials (detailed view in Figure S12, Supporting Information), revealing that the CEI formation of both methods is comparable. This indicates that keeping the half-cells at a fixed potential for 24 h does not have a detrimental effect on the cycling performance, but can rather serve as an initial formation step.

3. Conclusion

The decomposition kinetics of the LPSCl|NCM-83 composite were quantitatively studied via SOC dependent studies, showing an exponential increase of the CEI growth rate from 3.7 to 3.9 V versus In/InLi. This strong rise in growth rate indicates a significant increase in electrolyte degradation. In addition, the cell cycling unveiled a plateau of the reached capacity at $\geq$3.8 V versus In/InLi, which is likely due to a limit of accessible lithium-ions within the cathode. Comparing the cycling performance with and without a prior potential hold shows no significant differences, unveiling that a potential hold does not have a strong impact on the cycling performance, while simultaneously offering important insights on the CEI growth rate. In addition, this work shows that a prior potential hold can be seen as a formation step to remove the typically found first cycle capacity drop in solid-state batteries. This work presents an efficient matrix for the comprehensive electrochemical analysis of novel materials and material combinations in solid-state batteries, while enabling a more precise identification of the optimal voltage range for solid-state battery materials. The approach offers a versatile tool for advancing the understanding and development of next-generation battery systems. The application of the matrix in this work reveals new insights into the complex interplay between SOC-dependent cycling, CEI growth rate, and transport dynamics. The findings contribute significantly to the understanding of performance-limiting mechanisms in sulfide-based solid-state systems.

4. Experimental Section

Synthesis and Characterization of the Solid Electrolyte

The synthesis of LPSCl was carried out under argon atmosphere in a glovebox ($H_2O < 0.5$ ppm, $O_2 < 0.1$ ppm). A stoichiometric ratio of lithium chloride LiCl (Alfa Aesar, 99.99%), lithium sulfide Li_2S (Alfa Aesar, 99.99%), and diphosphorus pentasulfide P_2S_5 (Sigma–Aldrich, 99%) was hand ground in an agate mortar for 15 min. Afterward, the mixture was pressed into pellets and filled into carbon-coated quartz ampoules (inner $Ø = 10–12$ mm), which have been dried prior for 2 h at 800 °C under dynamic vacuum. The ampoules were then sealed under vacuum, transferred into a tube furnace, and heated with a heating rate of 100 °C h^{-1} to 550 °C. Annealing of the pellets then took place for 2 weeks at 550 °C. After natural cool down and hand grinding for 15 min, the final product powder LPSCl was obtained and stored in a glovebox under argon atmosphere to prevent contact with oxygen or moisture. A BioLogic VMP–300 Potentiostat was used to determine the conductivity of the SE via EIS on 200 mg of LPSCl in a cell casing between two steel stamps as current collectors. In addition, the phase purity of LPSCl was verified by powder X-ray diffraction (Stoe STADI P, $2\theta = 10°–70°$, Cu Kα: $\lambda = 1.54$ Å) and Raman spectroscopy (Bruker Senterra Raman microscope, 532 nm excitation laser, 2 mW laser power, spectra range 47–1548 cm^{-1}, spectral resolution = 3–5 cm^{-1}). The full characterization can be found in the supplementary information (Figure S1, Supporting Information).

Preparation of the Cathode Composite

Commercially available $LiNi_{0.83}Co_{0.11}Mn_{0.06}O_2$ (NCM-83, MSE Supplies) was used in this work, dried in a Büchi B–585 glass oven at 250 °C in dynamic vacuum for 36 h prior to use. The cathode composite was produced by mixing NCM-83 and LPSCl (as prepared above) in a weight ratio of 70:30 in batches of 100 mg each via soft milling by using five ZrO_2 balls with a diameter of 5 mm in 15 mL cups for 15 min at 15 Hz in a frequency shaker mill (Fritsch pulverisette 23 Mini Mill).

Cell Assembly

All solid-state battery half-cells[36] were built inside a glovebox under argon atmosphere using airtight press cells in the cell configuration In/InLi|LPSCl|NCM-83:LPSCl. First, 60 mg of LPSCl were filled in the cell as a separator and compacted using a hand press to archive a uniform layer. On one side of the separator, 12 mg of the cathode composite were evenly distributed. The two layers were then densified for 3 min with a uniaxial press using a pressure of three tons. Afterward, an indium foil (Ø = 9 mm; chemPUR; 100 μm thickness; 99.99%) was placed on the anode side. A freshly prepared lithium foil (1.5 mg; abcr; 99.8%) was placed on the center of this In foil. A constant pressure of 50 MPa during the electrochemical measurements via an Al frame. Before cycling, the cells were left to rest for 6 h at 25 °C to ensure pressure equilibration as well as InLi alloy formation.[37]

Cell Cycling

To investigate the influence of the SOC on the cycling stability over 50 cycles and the C-rate performance of an NCM-83:LPSCl (70:30 wt%) cathode composite in solid-state half-cells, six different upper cutoff potentials between 3.4 V and 3.9 V versus In/InLi in 0.1 V steps were used for all cell tests in this work, corresponding to 4.0 V and 4.5 V versus Li^+/Li. To assure reproducibility, triplicate measurements were carried out for each cutoff potential for long-term cycling and rate performance.[38] Both tests were conducted using a MACCOR (Series 4000) and carried out in a climate chamber (Binder) at 25 °C. The half-cells were cycled for 50 cycles in a potential window between 2.0 V versus In/InLi, corresponding to 2.6 V versus Li^+/Li, and one of the six predefined upper potentials applying a current density of $j = 0.214\ mA\ cm^{-2}$ (corresponding to a C-rate of 0.1 C). The rate performance tests were conducted in the same potential window using the C-rates C/20 ($0.107\ mA\ cm^{-2}$), C/10 ($j = 0.214\ mA\ cm^{-2}$), C/5 ($j = 0.428\ mA\ cm^{-2}$), C/2 ($j = 1.070\ mA\ cm^{-2}$), and 1 C ($j = 2.140\ mA\ cm^{-2}$). The stated current densities correspond to 8.4 mg of the CAM and were adjusted to the actual CAM masses of each cell. EIS measurements were performed at a BioLogic VMP–300 potentiostat in a climate chamber at 25 °C using an AC voltage of 10 mV in a frequency range of 7 MHz to 10 mHz. For EIS measurements, the half-cells were charged to one of the six upper cutoff potentials. The respective cutoff potential was held for 24 h, and during this time, EIS was carried out every 30 min. After the 24 h potential hold regime, the cells were cycled for 25 cycles, starting with a discharge to 2.0 V followed by a charge to the potential chosen for the 24 h potential hold, with EIS measurements recorded after each charge and discharge cycle. The RelaxIS3 software package (rhd instruments) was used for the evaluation and fitting of the impedance spectra.

Acknowledgements

The authors acknowledge the financial support by the German Federal Ministry of Research, Technology and Space (BMFTR, project BiSSFest 03XP0412G).

Open Access funding enabled and organized by Projekt DEAL.

Conflict of Interest

The authors declare no conflict of interest.

Author Contributions

Melina Witt: data curation (lead); writing—original draft (lead). **Martin A. Lange**: formal analysis (supporting); writing—review and editing (supporting). **Wolfgang Zeier**: conceptualization (lead); project administration (lead); resources (lead); validation (lead); writing—review and editing (lead).

Data Availability Statement

The data supporting this work is available on the research data repository of the University of Münster at https://doi.org/10.17879/22998615411.

Keywords: cathode electrolyte interphase · impedance · NCM · solid-state batteries · sulfide solid electrolytes

[1] J. Janek, W. G. Zeier, *Nat. Energy* **2023**, *8*, 230.
[2] S. Randau, D. A. Weber, O. Kötz, R. Koerver, P. Braun, A. Weber, E. Ivers-Tiffée, T. Adermann, J. Kulisch, W. G. Zeier, F. H. Richter, J. Janek, *Nat. Energy* **2020**, *5*, 259.
[3] A. M. Bates, Y. Preger, L. Torres-Castro, K. L. Harrison, S. J. Harris, J. Hewson, *Joule* **2022**, *6*, 742.
[4] C. C. Liang, *J. Electrochem. Soc.* **1973**, *120*, 1289.
[5] A. Mei, X. Wang, Y. Feng, S. Zhao, G. Li, H. Geng, Y. Lin, C. Nan, *Solid State Ionics* **2008**, *179*, 2255.
[6] A. Banik, B. Samanta, B. Helm, M. A. Kraft, Y. Rudel, C. Li, M. R. Hansen, B. V. Lotsch, S. Bette, W. G. Zeier, *Inorg. Chem.* **2024**, *63*, 8698.
[7] T. Zhao, A. N. Sobolev, X. Martinez de Irujo Labalde, M. A. Kraft, W. G. Zeier, *J. Mater. Chem. A* **2024**, *12*, 7015.
[8] L. Hu, J. Wang, K. Wang, Z. Gu, Z. Xi, H. Li, F. Chen, Y. Wang, Z. Li, C. Ma, *Nat. Commun.* **2023**, *14*, 3807.
[9] Y. Tanaka, K. Ueno, K. Mizuno, K. Takeuchi, T. Asano, A. Sakai, *Angew. Chem., Int. Ed. Engl.* **2023**, *62*, e202217581.
[10] L. Zhou, N. Minafra, W. G. Zeier, L. F. Nazar, *Acc. Chem. Res.* **2021**, *54*, 2717.
[11] S. Boulineau, M. Courty, J.-M. Tarascon, V. Viallet, *Solid State Ionics* **2012**, *221*, 1.
[12] T. Jeon, G. H. Cha, S. C. Jung, *J. Mater. Chem. A* **2024**, *12*, 993.
[13] W. Li, E. M. Erickson, A. Manthiram, *Nat. Energy* **2020**, *5*, 26.
[14] M. Bianchini, M. Roca-Ayats, P. Hartmann, T. Brezesinski, J. Janek, *Angew. Chem., Int. Ed. Engl.* **2019**, *58*, 10434.
[15] J. Ahn, J. Im, H. Seo, S. Yoon, K. Y. Cho, *J. Power Sources* **2021**, *512*, 230513.
[16] Y. Zhu, X. He, Y. Mo, *ACS Appl. Mater. Interfaces* **2015**, *7*, 23685.
[17] W. D. Richards, L. J. Miara, Y. Wang, J. C. Kim, G. Ceder, *Chem. Mater.* **2016**, *28*, 266.
[18] F. Walther, R. Koerver, T. Fuchs, S. Ohno, J. Sann, M. Rohnke, W. G. Zeier, J. Janek, *Chem. Mater.* **2019**, *31*, 3745.
[19] T.-T. Zuo, R. Rueß, R. Pan, F. Walther, M. Rohnke, S. Hori, R. Kanno, D. Schröder, J. Janek, *Nat. Commun.* **2021**, *12*, 6669.
[20] Y. Zhu, X. He, Y. Mo, *J. Mater. Chem. A* **2016**, *4*, 3253.

[21] J. Auvergniot, A. Cassel, J.-B. Ledeuil, V. Viallet, V. Seznec, R. Dedryvère, *Chem. Mater.* **2017**, *29*, 3883.

[22] X. Zhou, B. Zhang, P. Lyu, L. Xi, F. Li, Z. Ma, M. Zhu, J. Liu, *Energy Environ. Sci.* **2024**, *17*, 8174.

[23] D. H. S. Tan, E. A. Wu, H. Nguyen, Z. Chen, M. A. T. Marple, J.-M. Doux, X. Wang, H. Yang, A. Banerjee, Y. S. Meng, *ACS Energy Lett.* **2019**, *4*, 2418.

[24] H.-H. Sun, A. Manthiram, *Chem. Mater.* **2017**, *29*, 8486.

[25] R. Koerver, F. Walther, I. Aygün, J. Sann, C. Dietrich, W. G. Zeier, J. Janek, *J. Mater. Chem. A* **2017**, *5*, 22750.

[26] J. Hartel, A. Banik, M. Y. Ali, B. Helm, K. Strotmann, V. Faka, O. Maus, C. Li, H. Wiggers, W. G. Zeier, *Chem. Mater.* **2024**, *36*, 10731.

[27] Y. Morino, *J. Power Sources* **2022**, *541*, 231672.

[28] J. Kasnatscheew, M. Evertz, B. Streipert, R. Wagner, R. Klöpsch, B. Vortmann, H. Hahn, S. Nowak, M. Amereller, A.-C. Gentschev, P. Lamp, M. Winter, *Phys. Chem. Chem. Phys.: PCCP* **2016**, *18*, 3956.

[29] R. Ruess, S. Schweidler, H. Hemmelmann, G. Conforto, A. Bielefeld, D. A. Weber, J. Sann, M. T. Elm, J. Janek, *J. Electrochem. Soc.* **2020**, *167*, 100532.

[30] L. Ketter, N. Greb, T. Bernges, W. G. Zeier, *Nat. Commun.* **2025**, *16*, 1411.

[31] R. Tian, S.-H. Park, P. J. King, G. Cunningham, J. Coelho, V. Nicolosi, J. N. Coleman, *Nat. Commun.* **2019**, *10*, 1933.

[32] T. Bernges, L. Ketter, B. Helm, M. A. Kraft, K. A. See, W. G. Zeier, *EES Batter.* **2025**, *1*, 172.

[33] E. Schlautmann, J. Drews, L. Ketter, M. A. Lange, T. Danner, A. Latz, W. G. Zeier, *ACS Energy Lett.* **2025**, *10*, 1664.

[34] J. Ruhl, L. M. Riegger, M. Ghidiu, W. G. Zeier, *Adv. Energy Sustain. Res.* **2021**, *2*, 2000077.

[35] T.-T. Zuo, F. Walther, J. H. Teo, R. Rueß, Y. Wang, M. Rohnke, D. Schröder, L. F. Nazar, J. Janek, *Angew. Chem.* **2023**, *135*, e202213228..

[36] W. Zhang, D. A. Weber, H. Weigand, T. Arlt, I. Manke, D. Schröder, R. Koerver, T. Leichtweiss, P. Hartmann, W. G. Zeier, J. Janek, *ACS Appl. Mater. Interfaces* **2017**, *9*, 17835.

[37] A. L. Santhosha, L. Medenbach, J. R. Buchheim, P. Adelhelm, *Batteries Supercaps* **2019**, *2*, 524.

[38] S. Puls, E. Nazmutdinova, F. Kalyk, H. M. Woolley, J. F. Thomsen, Z. Cheng, A. Fauchier-Magnan, A. Gautam, M. Gockeln, S.-Y. Hasan, M.-G. Jeong, D. Hiraoka J.-S. Kim T. Kutsch, B. Lelotte, P. Minnmann, V. Miß K. Motohashi D. L. Nelson F. Ooms F. Piccolo C. Plank, M. Rosner E. Schlautmann R. Schuster, D. Spencer-Jolly, Y. Sun B. S. Vishnugopi, R. Zhang, et al. *Nat. Energy* **2024**, *9*, 1310.

Manuscript received: June 12, 2025
Revised manuscript received: July 11, 2025
Version of record online: July 24, 2025